Supplementary Information for "Photoacoustic Studies of Energy Transfer from Ozone Photoproducts to Bath Gases following Chappuis Band Photoexcitation"

Michael I. Cotterell,[1]* Kate Szpek,[2] David A. Tiddeman,[2] Jim M. Haywood[2,3] and Justin M. Langridge[2]

[1]School of Chemistry, University of Bristol, Bristol, UK, BS8 1TS

[2]Observation Based Research, Met Office, Exeter, UK, EX1 3PB

[3]College for Engineering, Mathematics and Physical Sciences, University of Exeter, Exeter, UK, EX4 4QF

* Author for correspondence: m.cotterell@bristol.ac.uk

Contents

S1. Pressure Dependent Processes during Photoacoustic Transduction

(1) Laser absorption by analyte:

$$\ln(I/I_0) = -\alpha_{abs}l$$

(2) Under assumption that all absorbed energy rapidly transfers to kinetic energy of the bath gas, the heat deposited in the gas is given by:

$$H(\vec{r}) = I_0 g(\vec{r})\alpha_{abs}$$

(3) Heat deposition generates an acoustic pressure wave that is then amplified by a photoacoustic cell. This amplified wave is given by:

$$|p| \propto \alpha_{abs}\frac{Q_n}{\omega_n}$$

in which both Q_n and ω_n depend on the equilibrium pressure P_0.

(4) The amplified photoacoustic wave drives the displacement $\hat{x}$ of microphone membrane.

P_0 affects damping ratio ζ for membrane displacement.

(6) Microphone displacement is directly proportional to the recorded voltage V_{mic}.
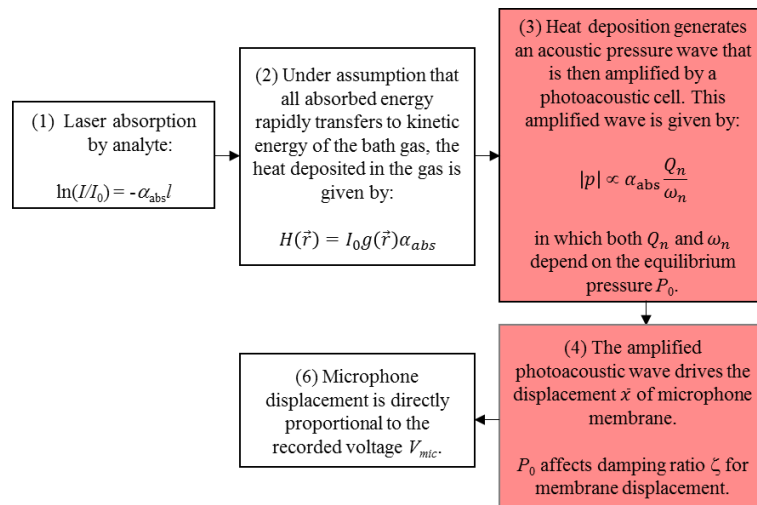
Figure S 1-1. The photoacoustic transduction process from laser light absorption by an analyte through to the recording of a microphone voltage response. Pressure dependent processes are highlighted in red text.
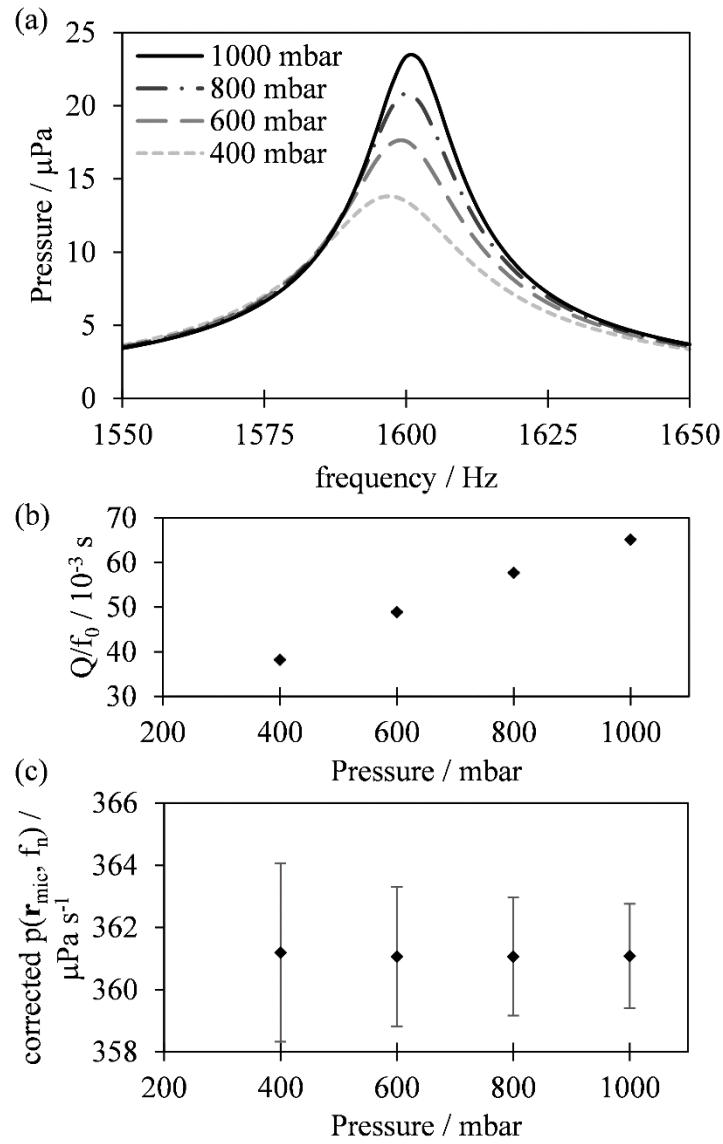
Figure S 1-2. (a) FEM model predictions of the frequency-dependent photoacoustic pressure amplitude at the microphone location $|p|$ with variation in the static pressure P_0 over the range $400 - 1000$ mbar. (b) and (c) show the variations in the cell time constant and the normalised photoacoustic signal ($|p|/(Q_n/\omega_n)$), respectively, with P_0.
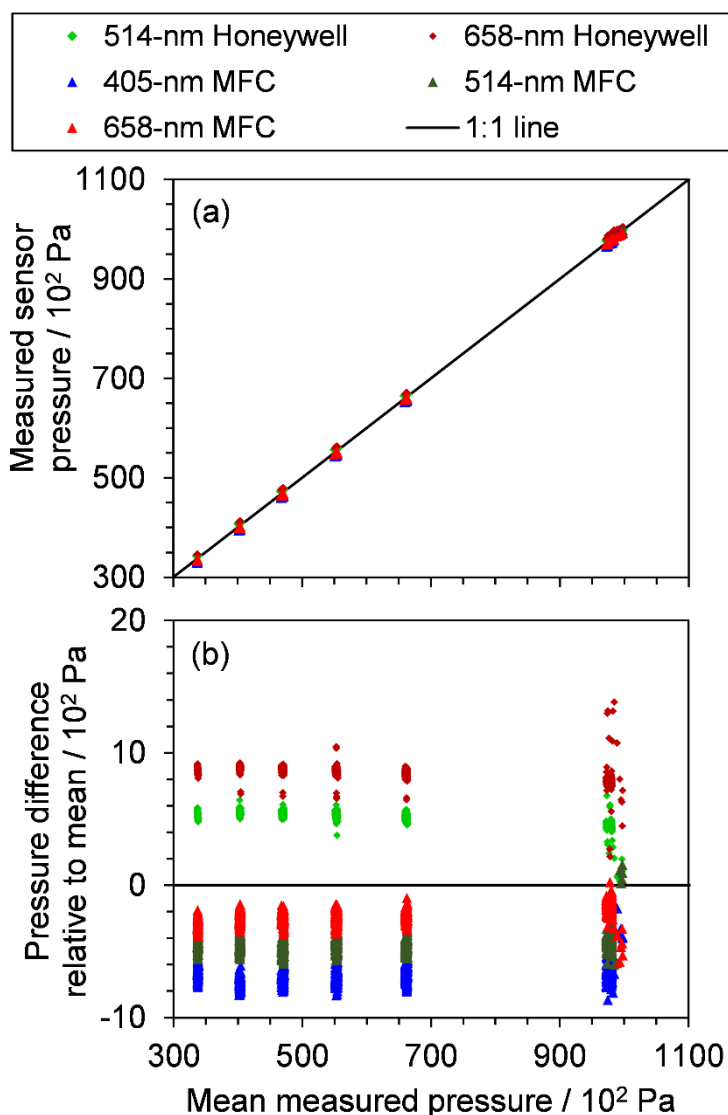
S2. Measurements of static sample pressure

Figure S 2-1. (a) Measurements of the static sample pressure from five separate pressure sensors integrated into our CRDS-PAS instrumentation as a function of the mean measured pressure from all five sensors. These sensors include three mass flow controllers that regulate the sample flow that is drawn through each spectroscopy flow line (labelled as 'MFC' in the figure legend), and two precision pressure transducers (Honeywell PPT-Series) that are located immediately after the 514 and 658-nm PAS instruments. (b) The difference in pressure recorded by each pressure sensor from the mean measured pressure from all five sensors, as a function of the mean measured pressure. The reduced pressure readings by the MFC sensors compared to those recorded by the Honeywell sensors are clearly shown; each MFC is located downstream of a HEPA filter that acts to impede the sample volumetric flow and thus causes a pressure drop downstream of the filter.

S3. Measurements of phase shift

The output power from the laser (Toptica, iBeam Smart) for the PAS spectrometer was modulated at a frequency f_{mod}, with f_{mod} the nearest integer value to the measured cell resonance frequency f_n, as determined by speaker-excitation measurements (see main text). The laser powers were modulated by supplying a sinusoidal waveform with a $0 - 5$ V DC peak-to-peak range to the analogue modulation terminal of each laser (referred to as the *laser modulation signal*). These waveforms directly control the laser power, with a maximum modulation frequency of 1 MHz. The modulation waveform is generated by a Field Programmable Gate Array (FPGA) card (National Instruments, PXI-7842R Virtex-5 LX50). The differential-amplified microphone response from the PAS spectrometer is acquired on the same FPGA card. Figure S 3-1 is a schematic to illustrate the waveforms for the laser modulation signal and the recorded microphone response. The microphone waveform has the same frequency as that of the modulation signal but is shifted in phase to later times. We examine the sources of this phase shift later in this section.
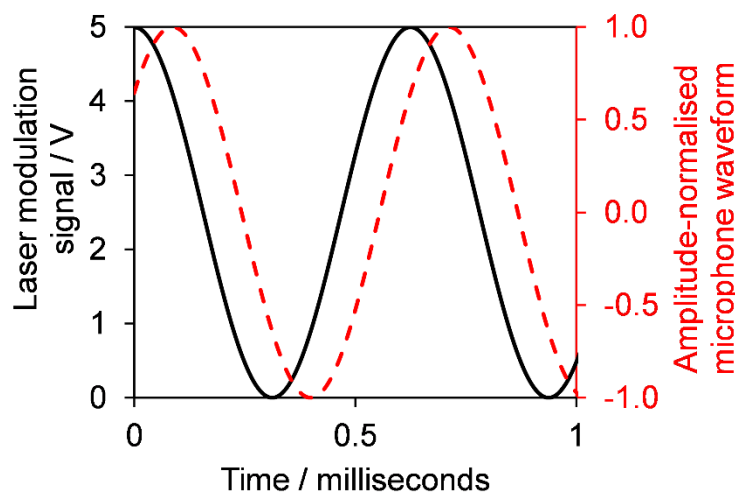

Figure S 3-1. Illustrative schematic to depict the phase shift in the recorded microphone waveform with respect to the laser modulation signal that is supplied to the analogue input to the PAS excitation laser.

The phase for each waveform is calculated in real time on the FPGA from the phase angle between the real and imaginary components of the FFTs for each waveform. These two phases are subtracted to give the raw phase shift, θ_{raw}. Figure S 3-2 shows variation in θ_{raw} during a single calibration; at the beginning of the calibration, a background phase is recorded corresponding to the PAS cell devoid of any light absorbing sample (red highlighted region at early times), before ozone-laden gas is introduced into the PAS cell and the concentration of ozone is then reduced in steps over time (yellow highlighted regions). The absence of θ_{raw} measurements between ozone concentrations arises because, prior to measurements of the background response and those at each ozone concentration, the acoustic amplification characteristics of the PAS cell (Q_n, f_n, S_{spk}) are measured by firing the speaker. During these speaker-

excitation measurements, θ_{raw} is not defined as the lasers are not providing excitation of the resonant mode during this time.
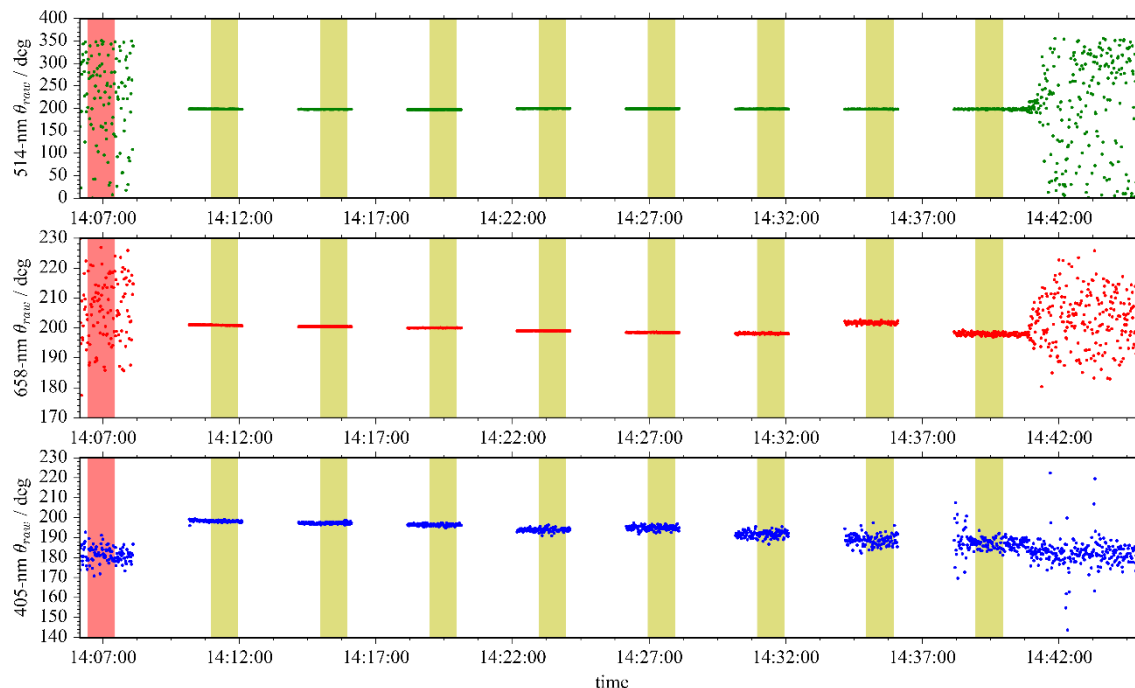

Figure S 3-2. The measured variation in θ_{raw} for each of our three PAS spectrometers during a single ozone calibration. At the beginning of the calibration (red rectangles), a background phase shift measurement is made for 30 s. Then, ozone-laden gas is introduced into the cell and is stepped to progressively lower concentration levels over time. At each of the eight ozone concentration levels supplied during a single calibration, the phase shift is measured for 30 s (yellow rectangles). This data set corresponds to measurements in a bath gas composition $x_{O_2} = 1.0$ and $P_0 = 304.1$ hPa.

During these calibrations, the resonance frequency changes with the ozone concentration. This change in f_n (in addition to Q_n and S_{spk}, see main text) is measured by exciting the cell with a speaker transducer. The determined f_n is used by a computer-controlled feedback to adjust the laser modulation frequency. However, our digitised output waveform for the laser modulation used a rounded (nearest integer) value for this frequency. This causes up to a 0.5 Hz discrepancy between the frequencies of the eigenmode resonances and that of the laser power modulation. Although this discrepancy may seem small, we show below that these differences in frequency cause significant changes in the measured phase shift. During calibrations, we record both the f_n (to a precision of eight decimal places) and the laser modulation frequency f_{mod}, and we use these frequencies to correct θ_{raw} during post-processing using the following treatment.

The frequency dependence of the excitation of the pressure eigenmode of the PAS cell is described by the equation (Cotterell et al., 2019b, 2019a; Miklós et al., 2001):

$$p(\vec{r}_M, \omega) = \sum_n \frac{i\omega}{\left(\omega_n^2 - \omega^2 + i\frac{\omega\omega_n}{Q_n}\right)} \frac{(\sigma - 1)I_0 \int g(\vec{r})\alpha_{abs}(\vec{r})p_n(\vec{r})dV}{V} p_n(\vec{r}_M)$$

in which ω_n is the angular frequency for the cell eigenmode ($\omega_n = 2\pi f_n$) and ω is the angular frequency at which the cell is being excited (in our case, $\omega = 2\pi f_{mod}$). For single mode excitation, the amplitude-normalised mode excitation distribution with frequency is described by a Lorentzian-like distribution of the form:

$$p(\vec{r}_M, \omega) = p_0 \frac{i\omega}{\left(\omega_n^2 - \omega^2 + i\frac{\omega\omega_n}{Q_n}\right)} \qquad \text{Eqn. S 3-1}$$

in which p_0 is the distribution amplitude and is associated with the overlap integral J_n ($J_n = \int g(\vec{r})\alpha_{abs}(\vec{r})p_n(\vec{r})dV$), eigenmode pressure at the microphone location ($p_n(\vec{r}_M)$), adiabatic coefficient (σ), laser intensity (I_0) and PAS cell volume (V). We calculate the additional phase shift (θ_L) introduced from the frequency mismatch between f_{res} and f_{mod} by inserting the measured f_n, Q_n and recorded f_{mod} into the Lorentzian distribution above (Eqn. S 3-1), and calculating the phase angle from the ratio of the imaginary and real components of $p(\vec{r}_M, \omega)$. We denote this added phase shift θ_L. Figure S 3-3 shows the amplitude $|p(\vec{r}_M, \omega)|$ of the distribution in Eqn. S 3-1 as a function of modulation frequency $f = \omega/(2\pi)$, in addition to the calculated phase shift θ_L, for typical f_n and Q_n of 1600 Hz and 90 respectively for our PAS cells. This figure demonstrates that a mismatch in the modulation frequency of ± 0.5 Hz with respect to the cell resonance frequency leads to errors in the recorded phase shift of up to $\theta_L \sim \pm 4\,°$.
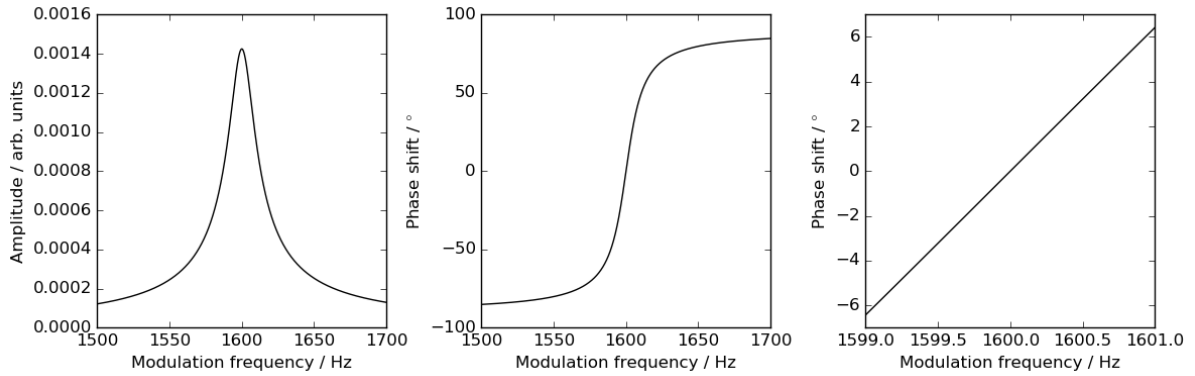

Figure S 3-3. Plots of the predicted amplitude and phase shift θ_L as a function of laser modulation frequency from Eqn. S 3-1 for a PAS cell with $f_n = 1600$ Hz and $Q_n = 90$.

Figure S 3-4 shows the predicted variation in θ_L for the data shown in Figure S 3-2. Variations in θ_L of approximately $\pm 2\,°$ are expected for this particular data set.
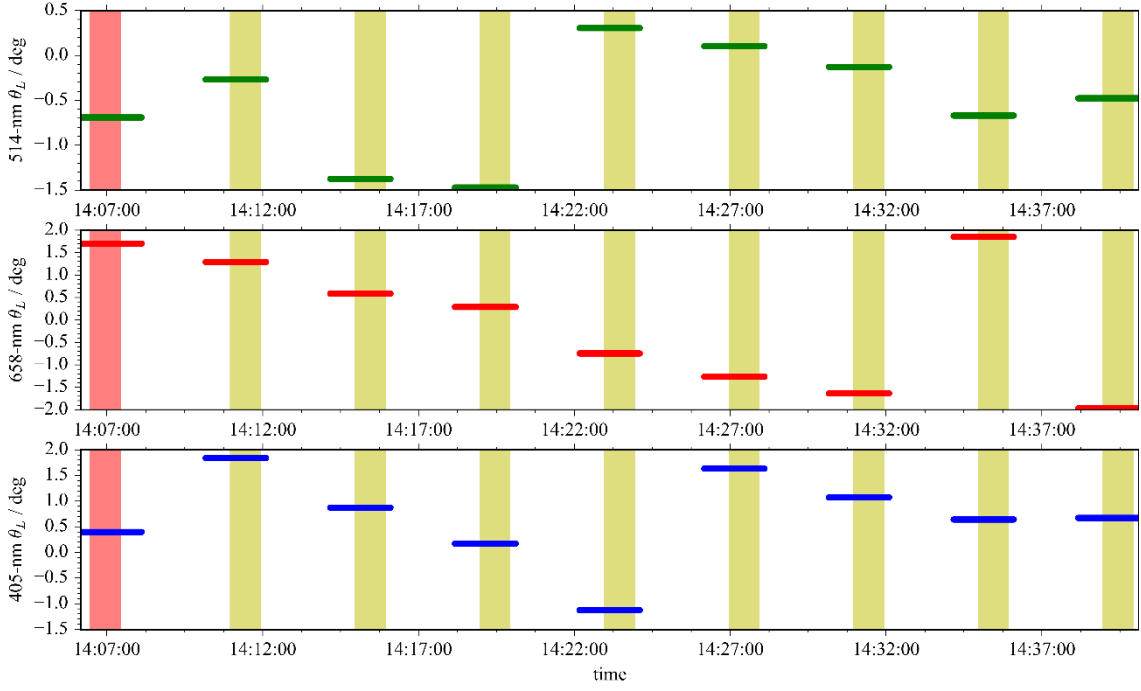
Figure S 3-4. For the same measurement data set presented in Figure S 3-2, this figure shows the predicted phase shift θ_L introduced by the mismatch between the PAS cell resonance frequency (f_n) and the modulation waveform used to drive the sinusoidal oscillation in the PAS cell laser power (f_{mod}).

We then subtract θ_L from θ_{raw} to give a corrected phase shift θ_{cor}. Figure S 3-5 shows the variation in θ_{cor} for the same calibration data set discussed above. Figure S 3-5 shows that the noise in θ_{cor} is higher when the ozone concentration is lower (i.e. at later times). For low sample absorption coefficients, the acoustic response at the microphone is low and the microphone signal is dominated by ambient acoustic noise, background contributions from laser-window interactions and electronic/microphone noise. To understand the measured variation in θ_{cor}, we can write this phase shift as a sum of both a constant instrument phase shift θ_{inst} (we will describe this contribution later in this section) and that from the photoacoustic wave driving a microphone response θ_{PA}:

$$\theta_{cor} = \theta_{inst} + \theta_{PA}$$

The phase θ_{PA} arises from two sources; the photoacoustic signal of interest from photoexcitation of ozone (with associated signal amplitude S_{sample}), and that from laser absorption by the windows of the PAS cell (with associated signal amplitude S_{bkg}). We can write the phase shift θ_{PA} as a sum of phases for the background and sample contributors weighted by their respective signal amplitudes:

$$\theta_{cor} = \theta_{inst} + \frac{S_{bkg}\theta_{bkg} + S_{sample}\theta_{sample}}{S_{bkg} + S_{sample}}$$

In the limit $S_{bkg} \ll S_{sample}$ and $S_{bkg}\theta_{bkg} \ll S_{sample}\theta_{sample}$:

$$\theta_{cor,max} = \theta_{inst} + \theta_{sample}$$

Therefore, in the limit of a strong PAS signal from O_3 absorption, the observed phase is independent of the background absorption from the PAS cell windows. For the same calibration set discussed above, Figure S 3-6 plots the measured phase with variation in the measured absorption coefficient for the ozone-laden sample; we note that the absorption cross section at $\lambda = 405$ nm is much lower than at the longer 514 and 658 nm wavelengths, resulting in a lower measured absorption at our shortest spectroscopy wavelength. This figure shows that, in the limit of large absorption (approximately for when $S_{sample}/S_{bkg} > 10$), the phase shift tends to a plateau at which the microphone signal is dominated by the sum of phases $\theta_{inst} + \theta_{sample}$.
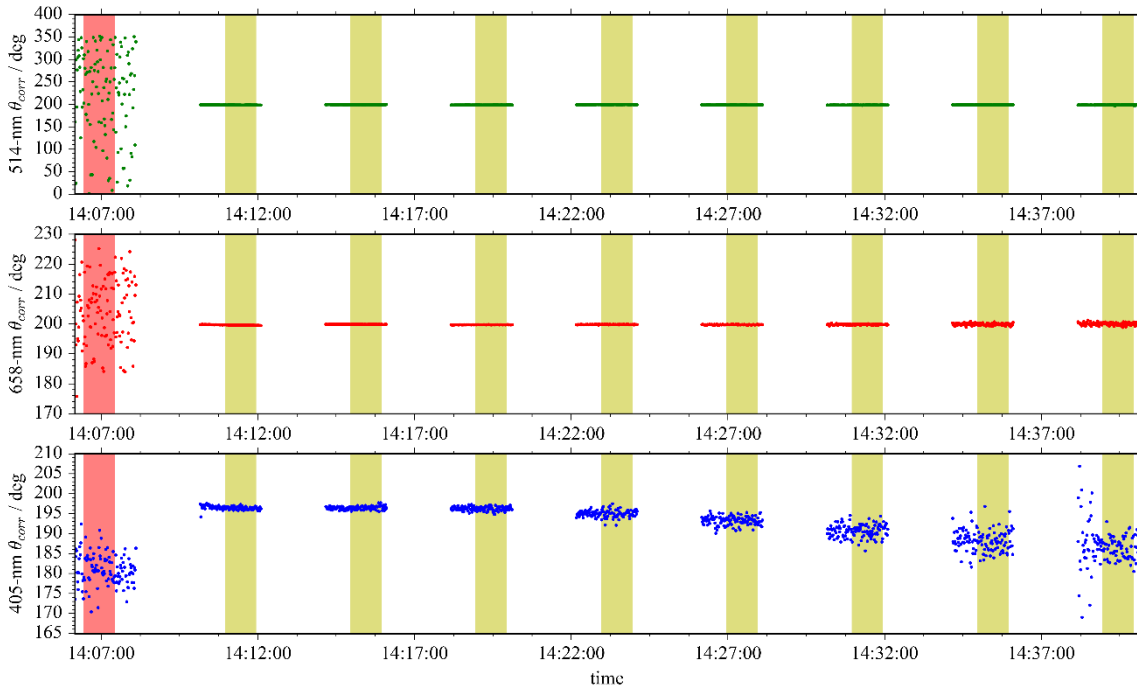

Figure S 3-5. For the same measurement data set presented in Figure S 3-2 and Figure S 3-4, this figure plots the corrected phase shift θ_{cor}.

Figure S 3-7 shows the variation in $\theta_{cor,max}$ for all our calibration data sets described in the main text, with $\theta_{cor,max}$ plotted as a function of the static pressure P_0 and different data series corresponding to the bath gas O_2 mass fraction (x_{O_2}). The data shows clear trends in the phase shift with both pressure and x_{O_2}, although there is a large systematic offset corresponding to the instrument phase shift θ_{inst}. The instrument phase shift arises from numerous sources. Kosterev et al., (2006) discuss sources of instrument phase shift in photoacoustic measurements. Sources relevant to our measurements include any delay in the response of the laser output power to the input analogue modulation waveform, phase

shift in the microphone response (e.g. a 90° phase shift could be envisaged if the microphone displacement is treated as an undamped simple harmonic oscillator), and delay in the microphone response waveform introduced by our differential amplification processing electronics prior to the FPGA data acquisition.
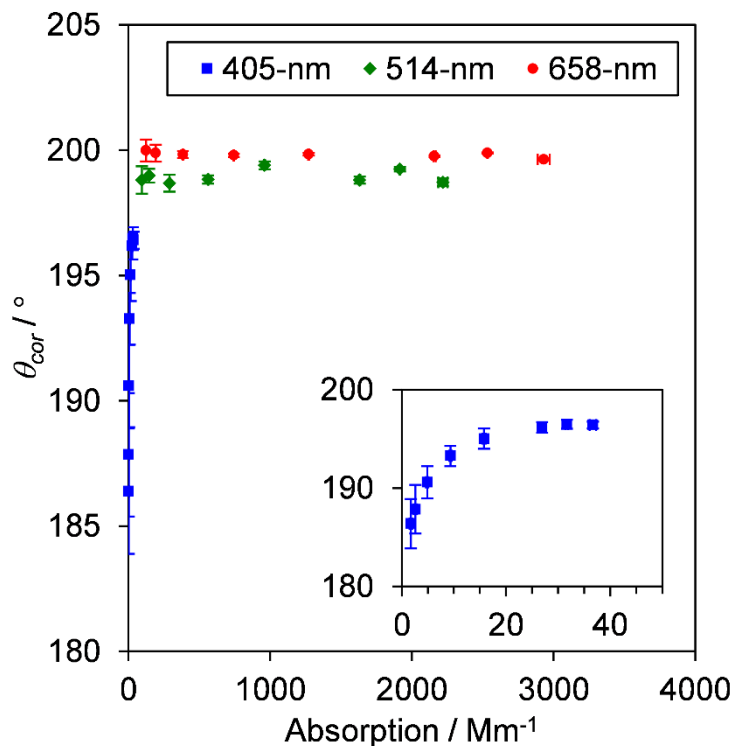

Figure S 3-6. The corrected phase shift θ_{cor} as a function of the measured absorption coefficient at each O_3 concentration level for the same measurement data set presented in Figure S 3-2, Figure S 3-4 and Figure S 3-5. The inset shows an expanded portion of the data set for measurements made by the 405-nm PAS instrument to highlight the tendency of θ_{cor} to trend towards a plateau for sample absorption values $> 20 \; \mathrm{Mm^{-1}}$.

To characterise θ_{inst}, we used a non-volatile aerosol sample with a sub-micrometre diameter; in the main text, we discuss that such an aerosol sample will not have a sample phase shift (θ_{sample}). Importantly, with a strong light absorbing sample, the microphone signal will be dominated by the contribution from the aerosol photoacoustic signal rather than the background arising from window heating. In this case, the measured θ_{cor} corresponds to θ_{inst}. Here, we used the same aerosol data set measurements described in Sect. 3.2 of the main text. Specifically, we examine here the measured phase shift when we passed monodisperse (250 nm diameter) dyed PSL aerosol through our PAS spectrometers. For these measurements, the absorption coefficient for the PSL sample ranged from 30 to 125 $\mathrm{Mm^{-1}}$ for measurements made across all the PAS spectrometers and over all P_0. Figure S 3-8 shows the measured θ_{cor} for our PSL measurements at six different values of static pressure over the range 330 – 1000 hPa. The θ_{cor} values are invariant with pressure and are the same for each

spectrometer within measurement uncertainty; θ_{inst} thus takes values of 190.6 ± 0.5 °, 189.5 ± 0.8 ° and 190.6 ± 0.4 ° for the 405-nm, 514-nm and 658-nm spectrometers respectively.
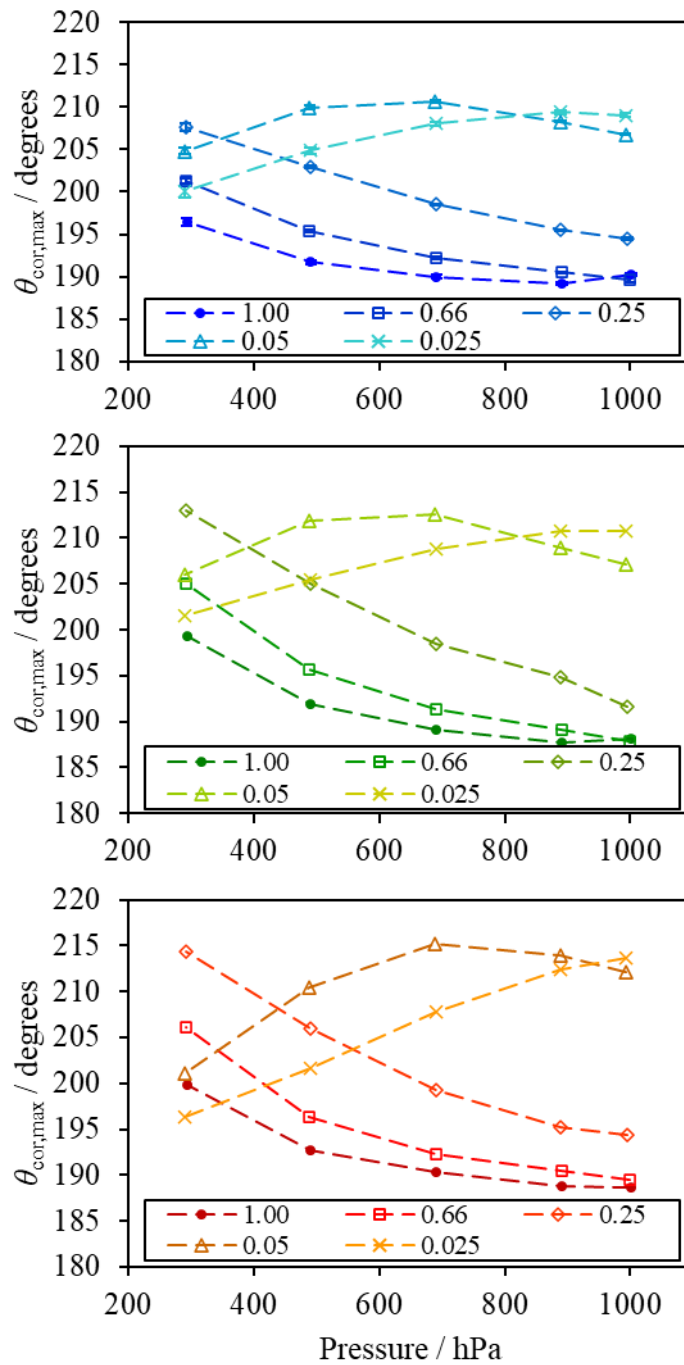

Figure S 3-7. The variation in $\theta_{cor,max}$ for all calibrations performed with the static pressure P_0. Different data series correspond to the different values of bath gas x_{O_2}. The top plot corresponds to measurements made at the 405 nm wavelength, the middle plot to measurements at 514 nm, and the bottom plot to measurements at 658 nm.
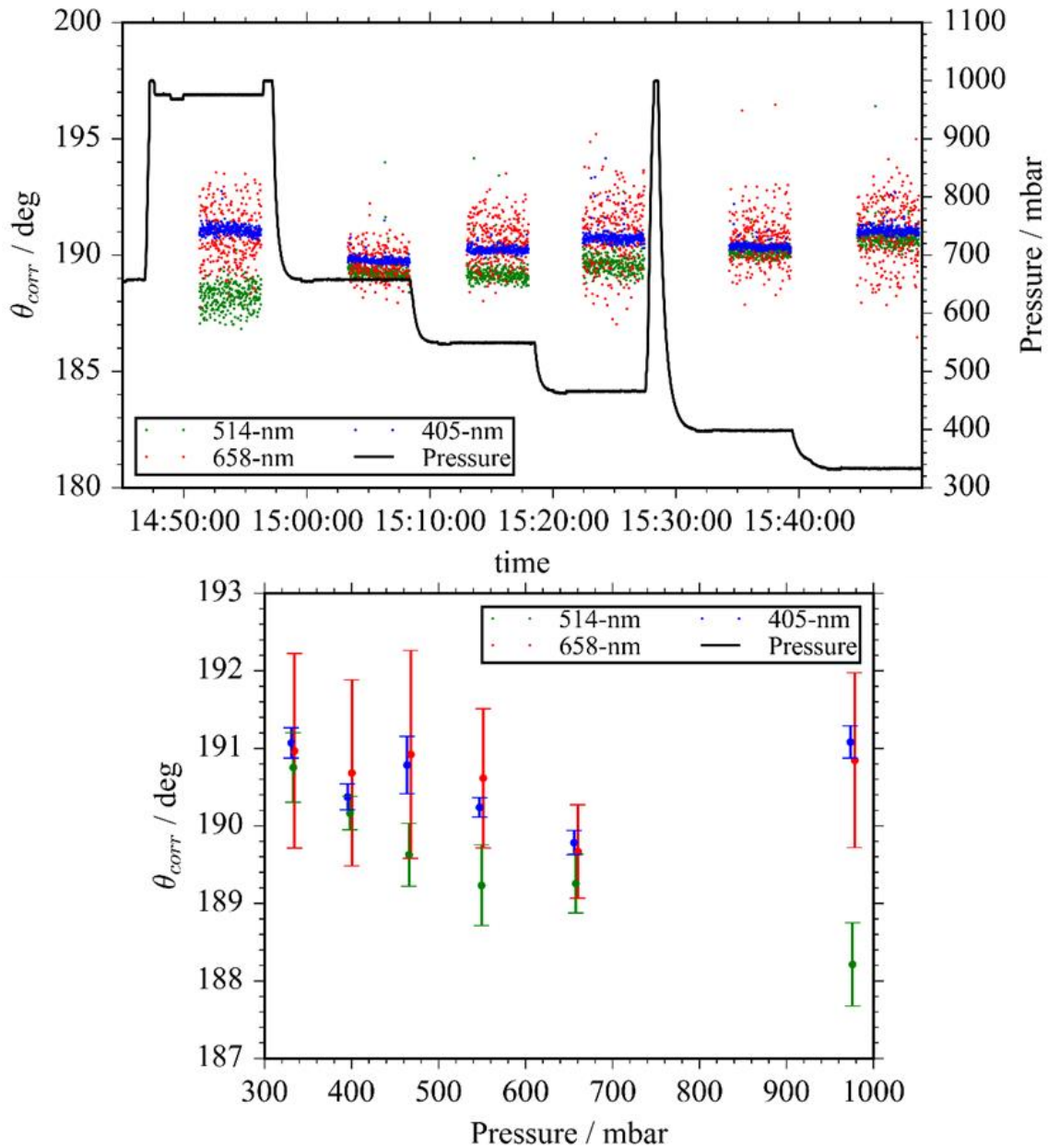
Figure S 3-8. (a) For measurements using each of our three PAS instruments, the measured θ_{cor} for 250 nm diameter dyed PSL spheres over time, with the pressure stepped to six different pressure levels over the duration of our measurements over the P_0 range 330 - 1000 hPa. At each pressure level, the phase shift was recorded for 5 minutes. (b) The mean θ_{cor} vs pressure for the same data as in (a).

Finally, the values for θ_{inst} for each PAS instrument, determined from our aerosol measurements, are subtracted from $\theta_{cor,max}$ for our ozone measurements to give θ_{sample}. Figure S 3-9 shows our measured variations in θ_{sample} with P_0 and x_{O_2}. These measured variations are discussed and modelled in the main text, in which θ_{sample} is referred to simply as the *phase shift*.
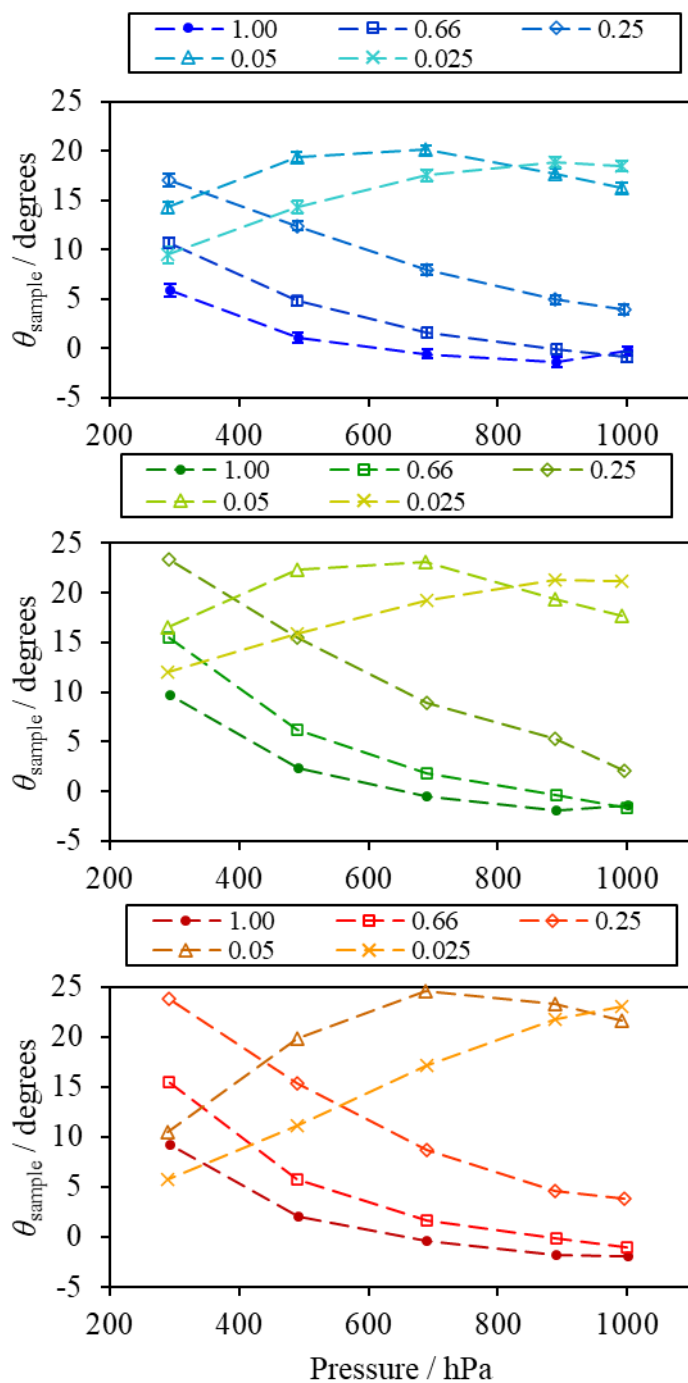
Figure S 3-9. The variation in θ_{sample} for all calibrations performed with the static pressure P_0. Different data series correspond to the different values of bath gas x_{O_2}. The top plot corresponds to measurements made at the 405 nm wavelength, the middle plot to measurements at 514 nm, and the bottom plot to measurements at 658 nm.

S4. Photoacoustic measurements for the detection of O₃ at visible wavelengths
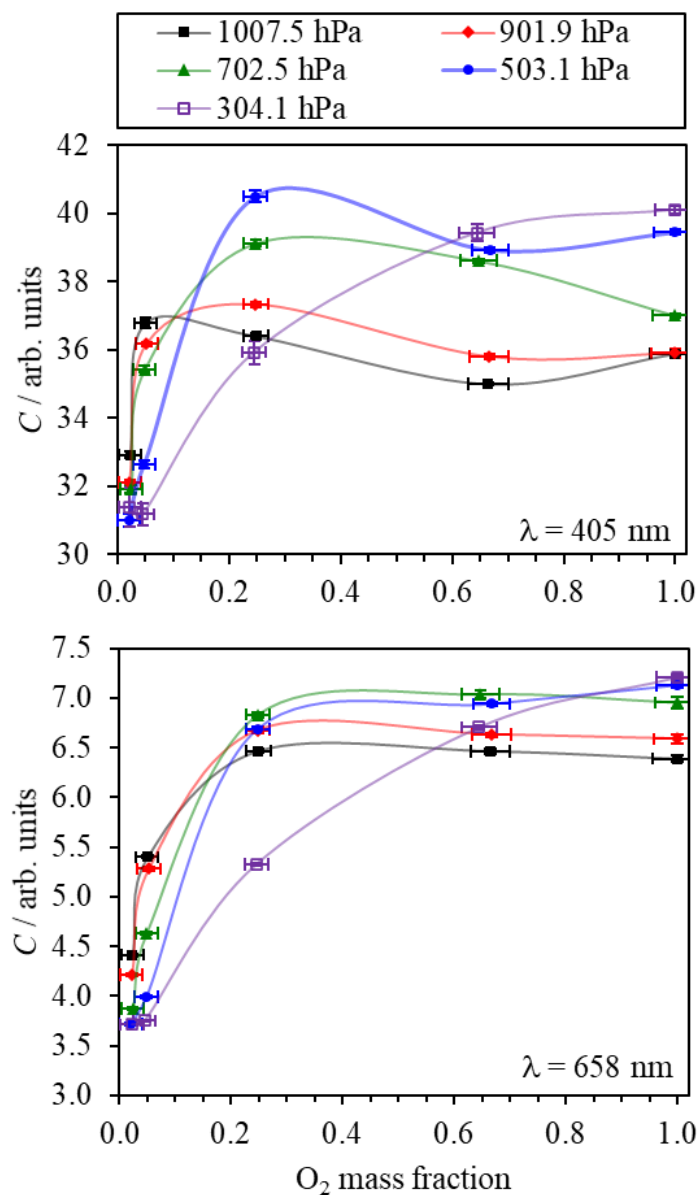

Figure S 4-1. The variation in the PAS sensitivity *C* (prior to any correction for microphone response function) with O₂ mass fraction for different static pressure levels. Measurements are shown for the 405-nm and 658-nm spectrometers. Lines are to guide the eye only.
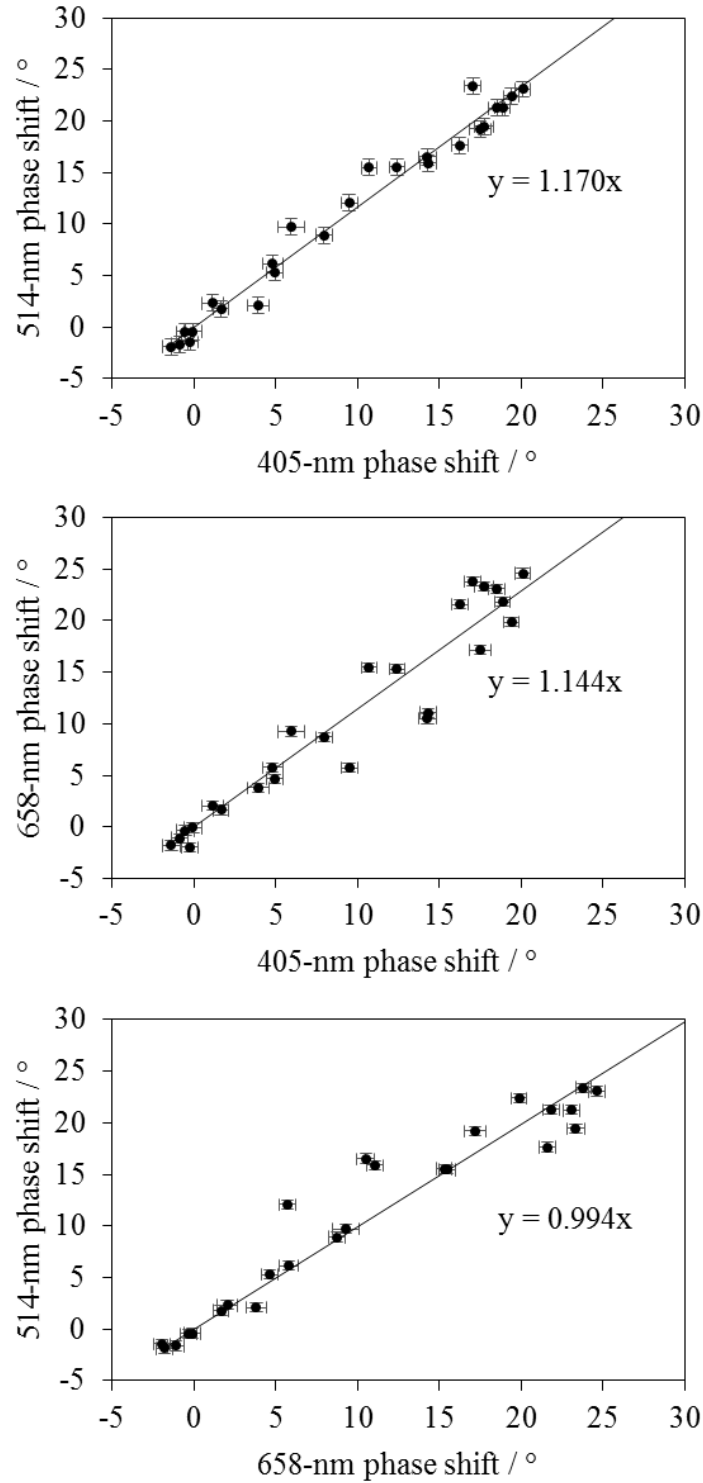
Figure S 4-2. Comparison of the measured photoacoustic phase shift from each spectrometer for corresponding values of P_0 and O_2 mass fraction. The solid line represents a least-squared fit of a straight line constrained through the origin, with the slope indicated on each plot. These slopes indicate that the phase shifts are near-identical for the 514 and 658-nm measurements, while the 405-nm measurements exhibit a reduced phase shift by ~13 – 15%.

S5. References

Cotterell, M. I., Ward, G. P., Hibbins, A. P., Haywood, J. M., Wilson, A. and Langridge, J. M.: Optimizing the performance of aerosol photoacoustic cells using a finite element model. Part 1: Method validation and application to single-resonator multipass cells, Aerosol Sci. Technol., 53(10), 1107–1127, doi:10.1080/02786826.2019.1650161, 2019a.

Cotterell, M. I., Ward, G. P., Hibbins, A. P., Wilson, A., Haywood, J. M. and Langridge, J. M.: Optimizing the performance of aerosol photoacoustic cells using a finite element model. Part 2: Application to a two-resonator cell, Aerosol Sci. Technol., 53(10), 1128–1148, doi:10.1080/02786826.2019.1648749, 2019b.

Kosterev, A. A., Mosely, T. S. and Tittel, F. K.: Impact of humidity on quartz-enhanced photoacoustic spectroscopy based detection of HCN, Appl. Phys. B Lasers Opt., 85(2–3), 295–300, doi:10.1007/s00340-006-2355-2, 2006.

Miklós, A., Hess, P. and Bozóki, Z.: Application of acoustic resonators in photoacoustic trace gas analysis and metrology, Rev. Sci. Instrum., 72(4), 1937–1955, doi:10.1063/1.1353198, 2001.